



**HAL**  
open science

## Innovative tail configuration : numerical VS wind tunnel test data

Sylvie Dequand, Arnaud Geeraert, Guy Mortchéléwicz

► **To cite this version:**

Sylvie Dequand, Arnaud Geeraert, Guy Mortchéléwicz. Innovative tail configuration : numerical VS wind tunnel test data. IFASD 2019, Jun 2019, SAVANNAH, United States. hal-02351334

**HAL Id: hal-02351334**

**<https://hal.science/hal-02351334>**

Submitted on 6 Nov 2019

**HAL** is a multi-disciplinary open access archive for the deposit and dissemination of scientific research documents, whether they are published or not. The documents may come from teaching and research institutions in France or abroad, or from public or private research centers.

L'archive ouverte pluridisciplinaire **HAL**, est destinée au dépôt et à la diffusion de documents scientifiques de niveau recherche, publiés ou non, émanant des établissements d'enseignement et de recherche français ou étrangers, des laboratoires publics ou privés.

# INNOVATIVE TAIL CONFIGURATION: NUMERICAL VS WIND TUNNEL TEST DATA

S. Dequand, A. Geeraert, and G. Mortchelewicz

ONERA, The French Aerospace Lab  
29 avenue de la Division Leclerc  
BP72, 92322 CHATILLON Cedex, FRANCE  
Sylvie.dequand@onera.fr

**Keywords:** aeroelasticity, high-fidelity simulations, flutter, empennage

**Abstract:** Aircrafts can be designed with different aft body configurations and all kinds of empennages exist. This paper focuses on the aeroelastic behavior of intersecting surfaces typically arising on aircraft tail, such as U-tail. It presents aerodynamic and flutter correlations between experimental and numerical results, in subsonic and transonic domains for a wind tunnel model representative of such aircraft tail. The aim is to evaluate the ability of our high-fidelity numerical tools to reproduce complex aerodynamic phenomena due to flow interactions between the different airfoil surfaces and to predict the sensitivity of the aeroelastic stability to the geometric parameters (dihedral, yaw angle).

Steady and unsteady pressure coefficients along different slices of the airfoil surfaces have been measured and are compared to numerically predicted pressure coefficients. Results obtained at different aerodynamic conditions provide a good insight of the effect of flow interactions between the intersecting airfoil surfaces. The aeroelastic stability of the flutter model is also investigated and allows the assessment of different numerical approaches by comparing their ability to predict flutter mechanisms.

## 1 INTRODUCTION

An aircraft tail is composed of a vertical and a horizontal empennage with fixed and movable parts which enable to control the aircraft stability in yaw and pitch, and the flight symmetry. Empennages with two or three vertical stabilizers are for instance often used for multi-engine aircrafts; twin-boom aircrafts are generally used in fret; other tail configurations are the T-tail, U-tail, V-tail, cross-tail and low-tail configurations. Innovative tail configurations are more and more considered with the objective of reducing noise and fuel consumption and an accurate understanding of the complex aerodynamic phenomena involved in such geometries with intersecting surfaces is needed. The subject of flow interaction between aircraft parts has become of interest since the 50s with the investigation of steady aerodynamic of wing-fuselage interaction [1], or VTP/HTP interaction ([2], [3]). The approaches for aeroelastic stability analysis are usually the Doublet Lattice Method (DLM) ([4], [5]) and also CFD-based aeroelastic simulations ([6], [7]).

In this paper, the study of innovative aft body configurations relies on a rich and thorough experimental database, allowing detailed data analysis of aeroelastic phenomena.

Preliminary comparisons between measurements on the U-tail configuration (Figure 1) and numerical results have already been presented in [8] and [9]. This paper will present

aerodynamic and flutter correlations between experimental and numerical results for a wind tunnel model representative of an aircraft U-tail. The aim of this study is to assess different numerical methods for the flutter analysis of tail configurations, in subsonic and transonic domains.

The first section of this paper will present a brief description of the Wind Tunnel Tests and the different geometries studied. Then, the different numerical methods used for the flutter analysis will be presented and finally, the results (pressure coefficients, flutter diagrams) will be shown in the last section.

## 2 WIND TUNNEL TESTS

The tail flutter model tests campaign with various geometric parameters and different aerodynamic conditions was performed in 2016 in the ONERA transonic pressurized wind tunnel S2MA, in the framework of the Cleansky research program, and thanks to a cooperation between RUAG, Dassault-Aviation and Onera. These Wind Tunnel Tests have received funding from the European Union's Seventh Framework Program (FP7/2007-2013) for the Clean Sky Joint Technology Initiative under grant agreement CSJU-GAM-SFWA-2008-001.

The flutter model was a bizjet type configuration, equipped with a large number of pressure sensors and accelerometers and was specially designed to investigate flutter mechanisms in subsonic and transonic domains. It was a 1/8 scale model wall-mounted in the wind-tunnel test section and consisted of a fixed fuselage and a half empennage geometry, as the U-tail shown in Figure 1. Different empennage geometries were investigated by varying dihedral and yaw angles of the vertical part.

Furthermore, different kinds of measurements were performed during the test campaign. A pitch motion could be applied to the model by means of a remotely controlled electro-hydraulic system. This so-called “pressure configuration” yielded to steady and unsteady aerodynamic data in order to calibrate numerical data.

For a given Mach number, the critical pressure was determined by continuously increasing the stagnation pressure. Several stabilized runs with stepping pressure were also recorded and analyzed to build the flutter curves. The Frequency Response Functions of the accelerometer responses during the stabilized runs were calculated relatively to the excitation actuator sensor and modal parameters were identified using the LMS Polymax software.

The flutter model was designed in such a way that the flutter mechanism was the result of a coupling between two structural modes, namely the first bending and torsion modes of the HTP.

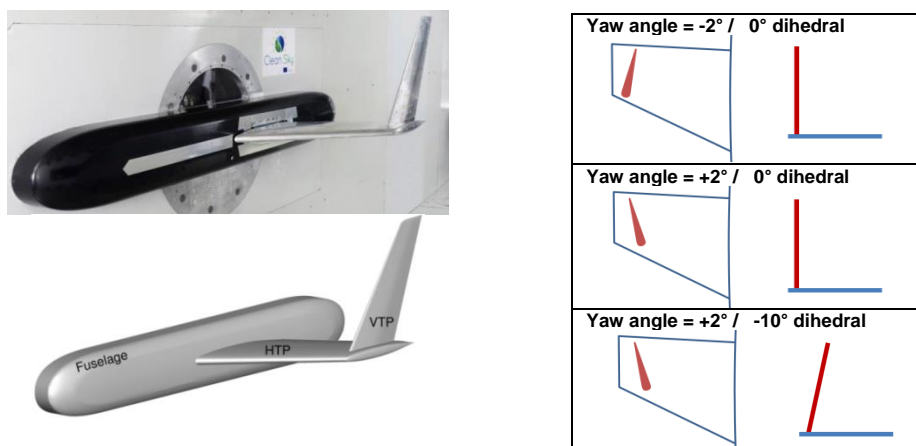


Figure 1: Flutter model wall-mounted in the WTT section. Scheme with notations and main geometric parameters considered in this paper.

### 3 NUMERICAL APPROACH

#### 3.1 Low-Fidelity coupling method

The flutter equation (1) is usually written in the Laplace domain using the Laplace variable  $p$ :

$$[p^2\mathbf{M} + p\mathbf{C} + \mathbf{K} - q_{dyn}\mathbf{GAF}(M, k)]\mathbf{X}(p) = 0 \quad (1)$$

where  $\mathbf{M}$ ,  $\mathbf{K}$ ,  $\mathbf{C}$  are respectively the modal mass, stiffness and damping matrices,  $\mathbf{GAF}$  is the matrix of Generalized Aerodynamic Forces,  $q_{dyn}$  is the freestream dynamic pressure,  $\mathbf{X}$  is the modal coordinate vector,  $M$  is the Mach number and  $k$  is the reduced frequency.

The usual approach in aircraft flutter prediction is to compute the Generalized Aerodynamic Forces (GAF) in the frequency domain and then to solve the aeroelastic stability problem using the classical double scanning “p-k” method ([10], [11]).

Most of the time, linear methods in frequency domain, such as the Doublet Lattice Method (DLM) [4], allow to compute the GAF and are valid in subsonic domain. This method is used in this paper and provides, additionally to the experimental database, an efficient comparison tool to validate our high-fidelity numerical methods, at least for low Mach numbers.

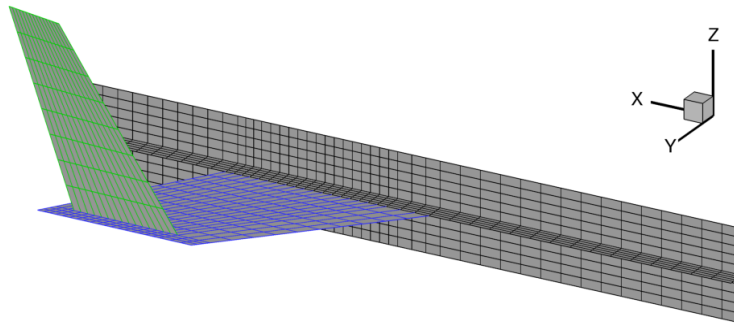


Figure 2: Aerodynamic panel mesh built for the DLM.

The aerodynamic mesh used in the DLM and shown in Figure 2, is made of different panels representing the different surfaces of the flutter model. The grey part corresponds to the fuselage (immobile part) and is made of a horizontal plane with  $46 \times 5$  panels and a vertical plane of  $46 \times 10$  panels. The blue part represents the HTP and is made of 21 chordwise panels and 13 spanwise panels. The green part corresponds to the VTP and is made of 15 chordwise panels and 8 spanwise panels. The structural mode shapes are projected onto these two parts by means of a finite volume fitting method. The mode shapes on the grey part are forced to zero by a locally smoothing technique applied at the junction between the grey and blue parts.

#### 3.2 High-fidelity method

High-fidelity simulations are performed with the elsA CFD code (Onera-Airbus-Safran property) [12], using its aeroelastic module “elsA-Ael”. The aeroelastic computations are based on a modal approach for the structure. The URANS computations are performed with a centered finite-volume discretization on a structured mesh, a backward-Euler scheme with implicit LUSSOR relaxation for time integration, and a 2<sup>nd</sup> order central Jameson scheme for spatial discretization.

An aerodynamic mesh was built for each studied configuration. The meshes used for the high-fidelity fluid-structure coupling simulations are structured meshes of about 8 millions mesh cells which are cut into a large number of blocks in order to use a maximum of processors and to reduce the CPU computation time. Figure 7 shows the wall surfaces of the U-tail

configuration. All the URANS computations have been performed with the Spalart-Allmaras turbulence model, for Mach numbers of 0.7 and 0.8. The walls of the wind tunnel were not modeled and only the wall on which the model was mounted was taken into account by applying a wall boundary condition on the grey boundary shown in Figure 7. All the other far-field mesh boundaries were set to non-reflective boundary conditions.

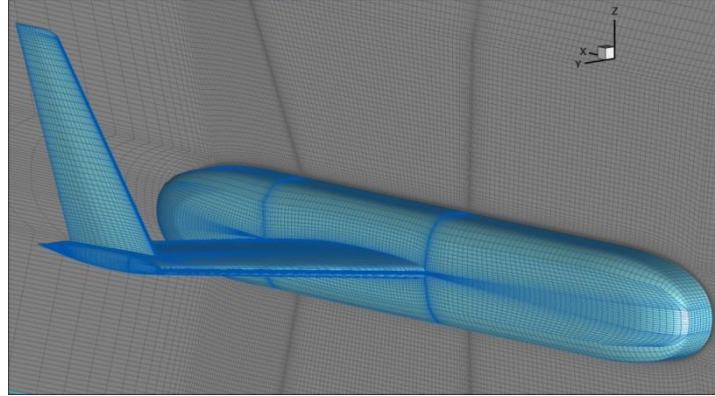


Figure 3: Aerodynamic structured mesh used in the Hi-Fi numerical simulations

### 3.2.1 Forced Harmonic Excitation method (FHEM)

GAF can be computed by evaluating the unsteady aerodynamic response to any admissible motion of the structure, considered to behave linearly, in the frequency range of interest of the problem. In this Forced Harmonic Excitation method, several numerical simulations are performed, for a set of structural modes and for various values of excitation frequencies. While very robust, this harmonic motion approach requires however one unsteady simulation for each structural mode and for each frequency selected in the frequency range of interest, and is therefore very time consuming.

### 3.2.2 Pulse method

In the so-called “Pulse” method ([13], [14], [15]), the forced motion is not harmonic in time anymore but corresponds to a Heaviside function (step function from 0 to 1, at a given initial instant, Figure 4), applied to a structural mode. With such an approach, the impulse response of the system is computed in a single simulation for a full frequency range.

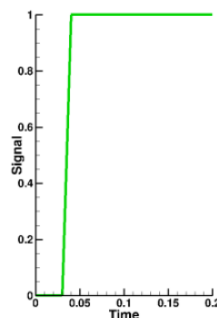


Figure 4: Step function used as excitation signal in the “Pulse” method.

The GAF can be written as a function of a transitory part  $T(i, t)$  and the impulse response  $h(i, j, t)$ :

$$GAF(i, j, n\Delta t) = T(i, n\Delta t) + e_0 \Delta t \sum_{k=0}^n h(i, j, k\Delta t) \quad (2)$$

where  $\Delta t$  is the time step,  $n\Delta t$  is the current time, and  $e_0$  is an amplification factor. The GAF can then be determined by means of a classical Fourier analysis of the time responses:

$$\hat{f}(\omega) \approx \Delta t \sum_{k=0}^n f(k\Delta t) e^{-i\omega k\Delta t} \quad (3)$$

In this paper, three different methods have been therefore used to compute the GAF of the flutter model: high-fidelity aeroelastic simulations based on the FHEM and the Pulse method, and the DLM. Figure 5 shows a comparison of the modulus and the phase of the GAF computed with these three methods for a given flutter model configuration. The GAF modulus obtained with the Pulse method and the FHEM are very similar but differ from the DLM results. A very good correlation is however obtained for the GAF phase and shows that the three methods are predicting the same aerodynamic behavior.

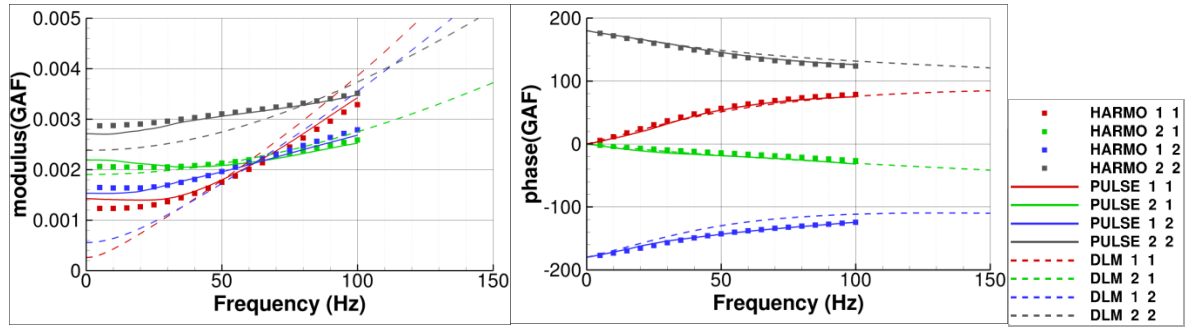


Figure 5: Mach = 0.7, Pi = 1.0 bar. GAF evolution with the frequency computed with three different methods: DLM, FHEM and Pulse. (Yaw angle =  $-2^\circ / 0^\circ$  dihedral)

### 3.2.3 Direct Coupling method (DCM)

An alternative approach to the previous presented methods (FHEM and Pulse method) is the so-called “Direct Coupling” method (DCM) in which several dynamic fluid-structure coupling simulations are performed at different stagnation pressure  $P_i$ , with an initial modal velocity applied to each structural mode. For the dynamic fluid-structure coupling simulations, the numerical technique consists in using an iterative process which is converged at each physical time-step. As schematically represented in Figure 6, the different steps performed at each time step are:

1. Computation of the flow solution (using a dual time-stepping technique)
2. Computation of the generalized aerodynamic loads (GAF)
3. Computation of the generalized coordinates, solving the mechanical modal system and using the implicit Newmark scheme for time discretization
4. Computation of the displacements of the aerodynamic surface grid, from the modal shapes and the generalized coordinates
5. Deformation of the aerodynamic grid

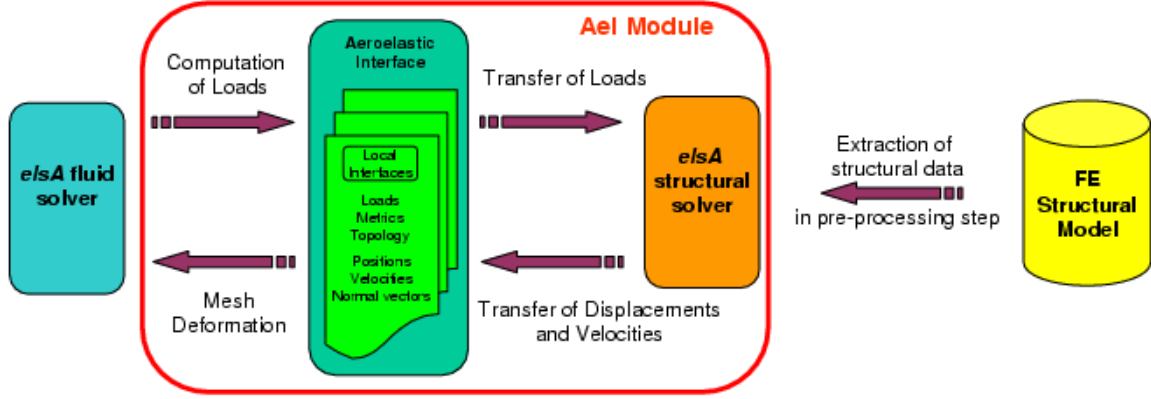


Figure 6: Aeroelastic optional subsystem of elsA for aeroelastic simulations

The generalized aerodynamic forces (GAF) are deduced from the aerodynamic flow field and computed by integration of the pressure field, directly on the aerodynamic wall grid since the structural mode shapes are projected to the aerodynamic surfaces in a pre-processing step by using interpolation or fitting techniques ( $\Phi_{S,i} \Rightarrow \Phi_{A,i}$ ):

$$gaf_i = \iint_{Wall} -p\vec{n}\vec{\Phi}_{A,i}dS \quad (4)$$

where  $\vec{\Phi}_{A,i}$ ,  $i=1,N$  are the  $N$  first mode shapes, mapped on the aerodynamic surface grid.

The generalized coordinates  $q_i$  are then computed from the dynamic modal system:

$$m_i\ddot{q}_i + 2m_i\alpha_i\omega_i\dot{q}_i + m_i\omega_i^2q_i = gaf_i \quad (i=1,N) \quad (5)$$

where  $m_i$  is the generalized mass,  $\omega_i$  the pulsation, and  $\alpha_i$  the structural damping coefficient.

The wall displacements and velocities,  $\Delta\vec{X}_A$ , and  $\Delta\dot{\vec{X}}_A$  are provided directly on the aerodynamic surface grid by:

$$\Delta\vec{X}_A(M,t) = \sum_{i=1}^N q_i(t)\vec{\Phi}_{A,i}(M), \quad \Delta\dot{\vec{X}}_A(M,t) = \sum_{i=1}^N \dot{q}_i(t)\vec{\Phi}_{A,i}(M) \quad (6)$$

For the deformation of the aerodynamic grid, an individual “modal mesh deformation” is first computed for each mode at the start of the coupled simulation, using a mixed analytical/transfinite interpolation technique. The instantaneous mesh deformation  $\Delta\vec{X}_A^n$  at time level  $n$  is then computed as a linear combination of these individual “modal” mesh deformations:

$$\Delta\vec{X}_A^n = \sum_{i=1}^N q_i^n \Delta\vec{X}_{A,i}^{\text{modal}} \quad (7)$$

where  $q_i^n$  are the generalized coordinates solution of the dynamic modal system.

At last, a coupling iteration loop between the two disciplines has been setup within the physical time loop in order to get a converged coupled fluid-structure state at each physical

time step. In practice, it is observed that two or three iterations are enough for most aeroelastic problems.

For each Pi, the time responses obtained with the DCM are assumed to be written as:

$$s(t) = C + \sum_{k=1}^N s_k(t) = C + \sum_{k=1}^N A_k \sin(\omega_k t + \phi_k) e^{-\alpha_k \omega_k t} \quad (8)$$

The set of parameters  $\{C, A_k, \omega_k, \alpha_k, \phi_k\}_{k=1}^N$  is estimated by a fitting procedure based on the Levenberg-Marquardt algorithm [16]. Figure 7 gives an example of a typical time response obtained and its Fourier signal processing. This Direct Coupling method enables to determine the critical stagnation pressure at which the system becomes unstable, but requires however several computations and can become very time consuming.

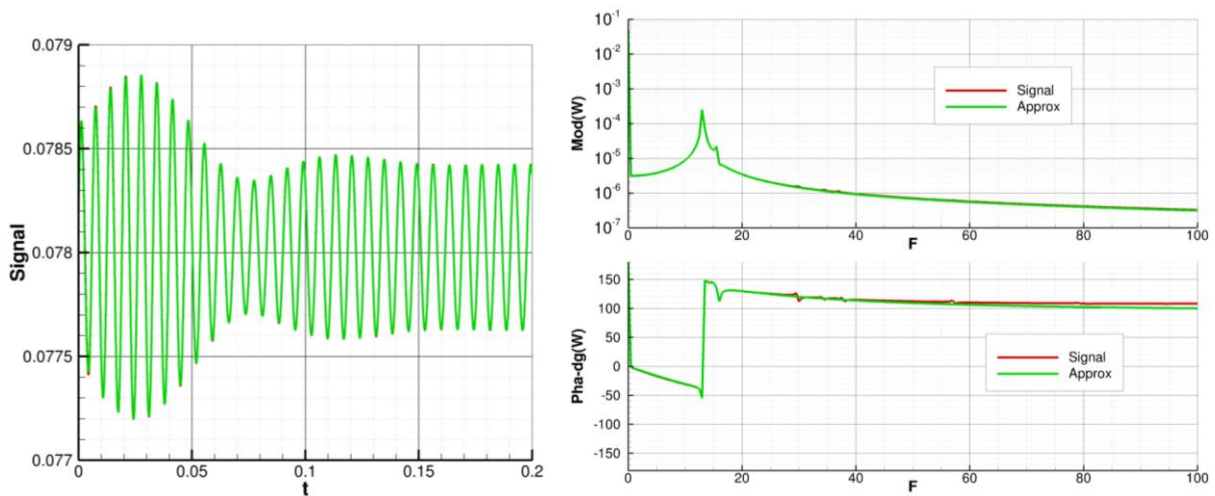


Figure 7: Examples of a time response and its Fourier signal processing.

## 4 RESULTS

### 4.1 Cp comparisons

#### 4.1.1 Steady pressure coefficients

The steady pressure coefficients have been measured at different slices over the horizontal and vertical tail planes (HTP and VTP) (Figure 8). These experimental data can be directly used to calibrate our numerical data.

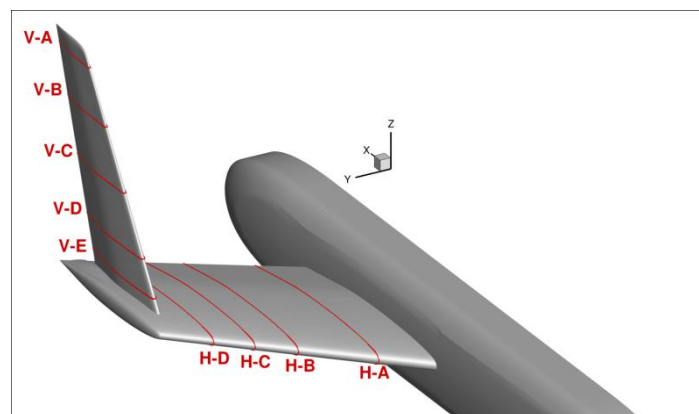


Figure 8: Location and notation of the different HTP and VTP slices

Static fluid-structure coupling URANS simulations have been performed using our high-fidelity CFD code elsA, in order to compare the numerical pressure coefficients to the measured steady pressure coefficients. Figure 9 shows the results obtained at Mach = 0.7 and  $P_i = 1.0$  bar with and without taking into account the structural deformation. The curves are respectively denoted ‘Static Coupling’ and ‘Rigid’ in the different graphs representing different slices over the HTP and the VTP of the model.

Contrary to the experimental steady pressure coefficients, the ‘Static Coupling’ pressure coefficients are different at the upper and lower HTP surfaces and show that the empennage numerically computed static deformation has a non-zero incidence. The comparison of the numerical static deformed empennage with the MDM data (Model Deformation Measurement) confirms indeed that the static deformation is not well predicted by our static aeroelastic simulations. This is due to the modal approach used, in which the structure is represented only by its first eleven modes. In a best practice, the static deformation should be computed by means of a flexibility matrix approach. However, this method requires a Finite Element Model of the structure, which was not available for this study. The MDM data show that the static deformation of the empennage is negligible (displacements lower than 0.5mm) and when considering the numerically predicted ‘Rigid’ pressure coefficients, a rather good correlation with the experimental data is indeed obtained at the different HTP and VTP slices.

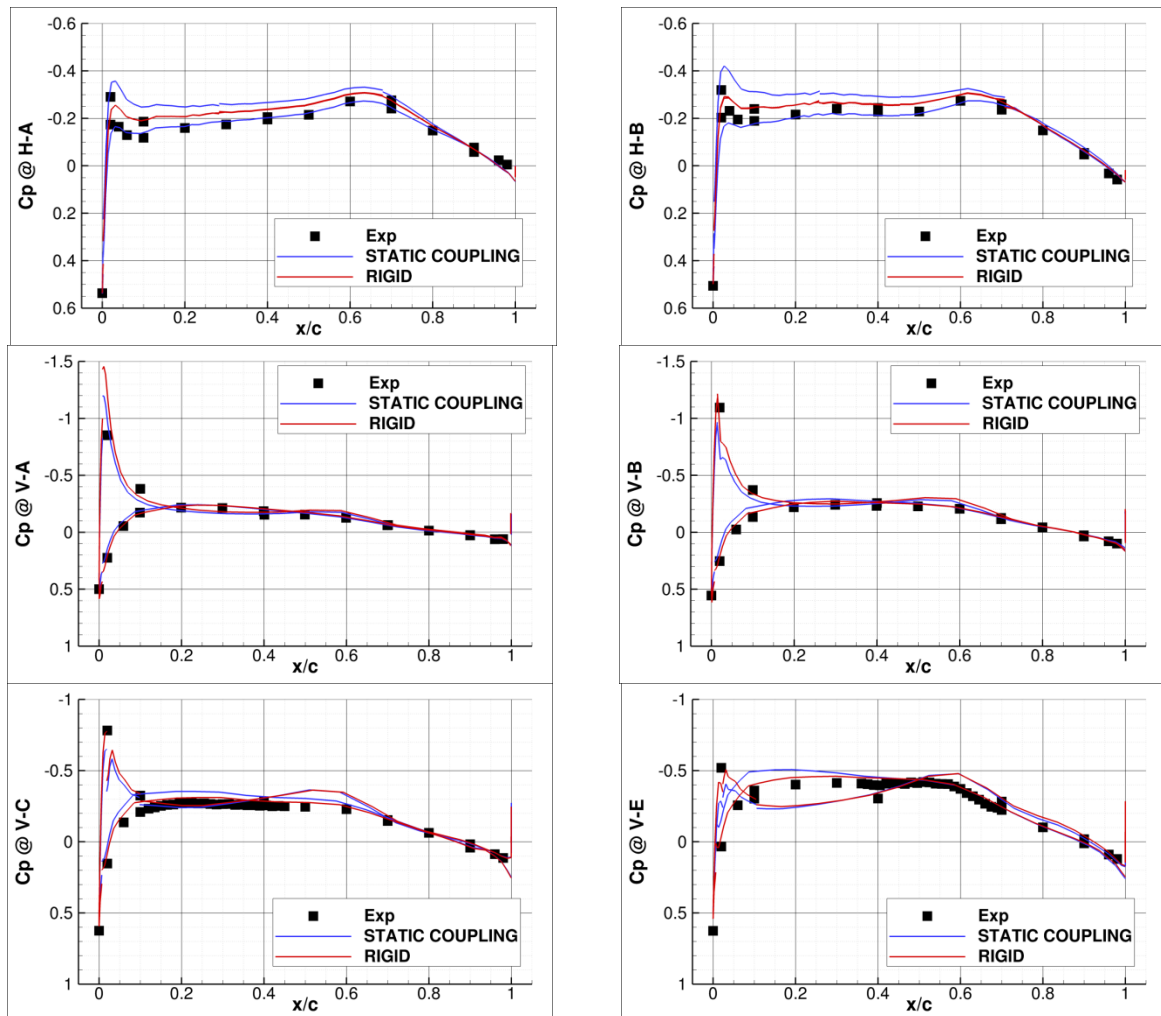


Figure 9: Experimental and numerical steady pressure coefficients on different HTP and VTP slices at Mach=0.7 and  $P_i = 1.0$  bar (Yaw angle =  $-2^\circ / 0^\circ$  dihedral)

Figure 10 shows the effect of a higher Mach number on the steady pressure coefficients obtained at the ‘H-A’ HTP slice, which corresponds to the slice located closer to the fuselage. The main difference is that the pressure is not well predicted from the last 20% of the HTP chord. This is probably due to a problem of leakages which occurred during the wind tunnel tests, at the junction between the fuselage and the HTP.

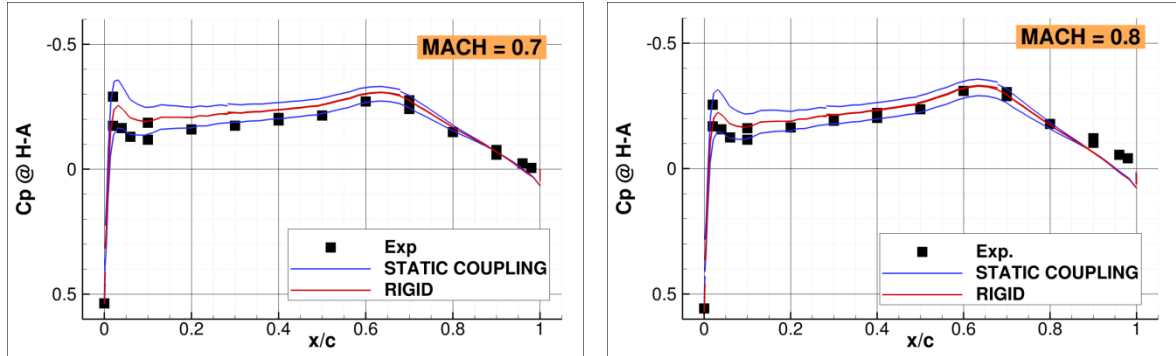


Figure 10: Mach effect on experimental and numerical steady pressure coefficients on the ‘H-A’ HTP slice (Yaw angle =  $-2^\circ / 0^\circ$  dihedral).

In order to take into account these leakages, a mass flow injection boundary condition is imposed at the first line of cells located on the fuselage around the HTP junction (thin white zone in the bottom right hand-side graph in Figure 11). This injection condition is defined as a blowing flow condition corresponding about to 5% of the flow velocity, towards the Y-direction. Figure 11 shows indeed that the injection boundary condition improves the prediction of the steady pressure coefficients.

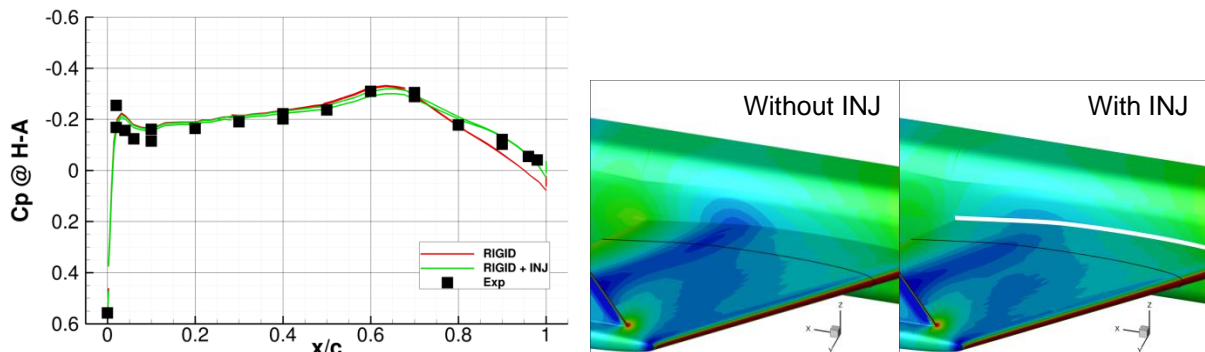


Figure 11: Effect of an injection condition at the junction between the fuselage and the HTP (Yaw angle =  $-2^\circ / 0^\circ$  dihedral). Pressure coefficients on the ‘H-A’ HTP slice and pressure field near the injection zone.

The next figures show the effect of a change in the empennage geometry on the pressure field. The geometrical parameters considered are the yaw angle and the dihedral. Figure 12 shows that a positive yaw angle changes completely the pressure field distribution over the VTP surface, with the apparition of a recompression, probably due to the VTP incidence. The negative dihedral increases this phenomenon.

Figure 13 shows the steady pressure coefficients at different HTP and VTP slices for positive and negative yaw angles. When the VTP is directed towards the fuselage (positive yaw angle), a shock on the VTP occurs. As shown in Figure 14, the effect of the dihedral is less spectacular. The steady pressure coefficients are very similar, with only a slight increase when the dihedral is negative (towards the fuselage).

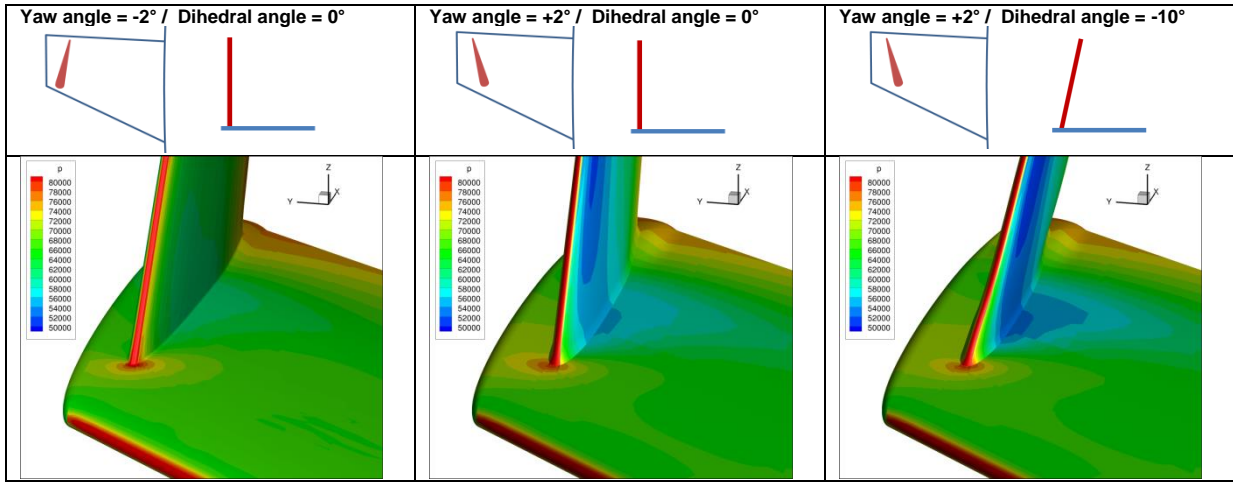


Figure 12: Effect of the yaw and dihedral angles on the steady pressure field at the cross section between HTP and VTP (Mach = 0.7 and  $P_i = 1.0$  bar).

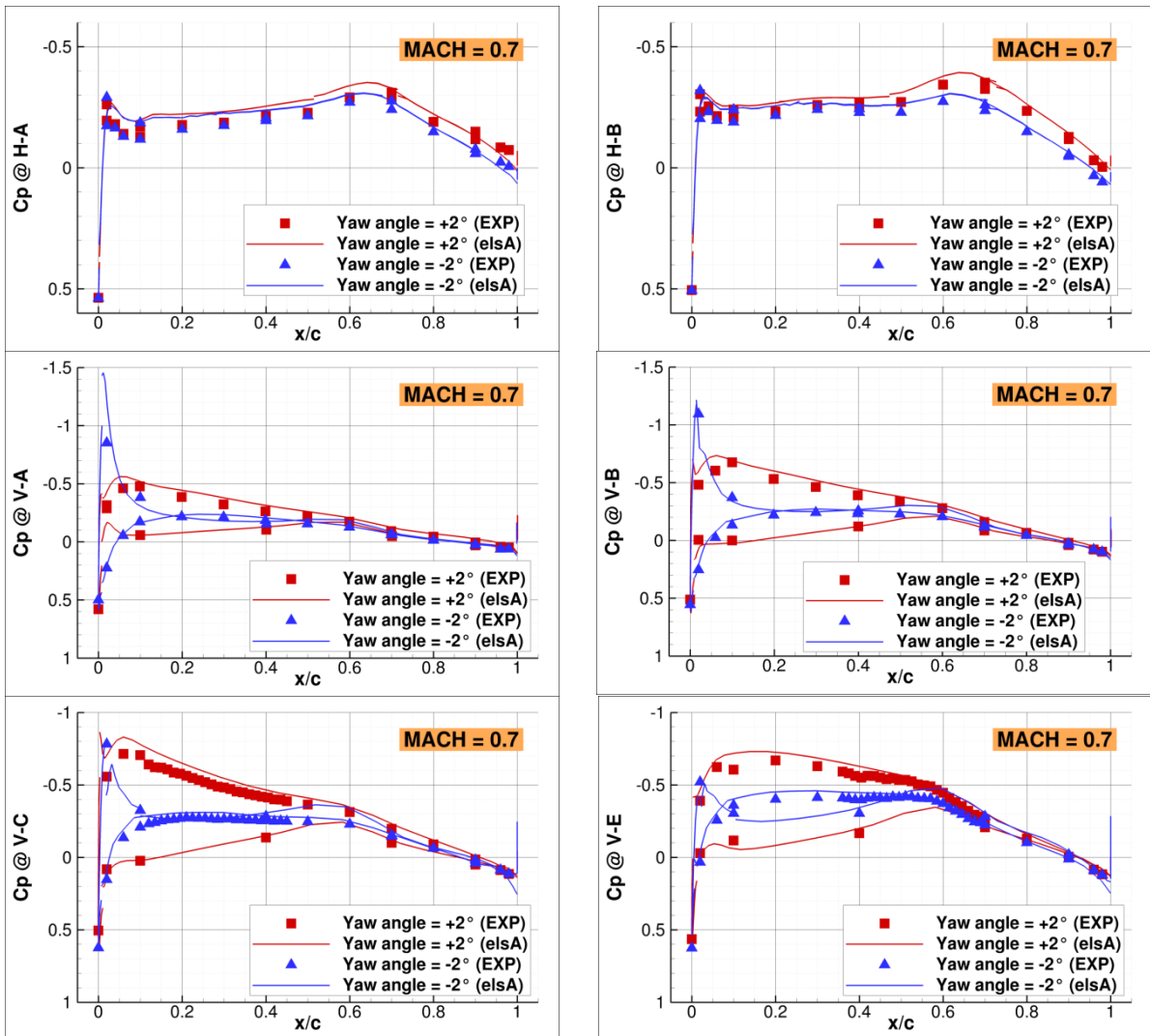


Figure 13: Yaw angle effect on experimental and numerical steady pressure coefficients on different HTP and VTP slices at Mach=0.7 and  $P_i = 1.0$  bar with a fixed dihedral of  $0^\circ$ .

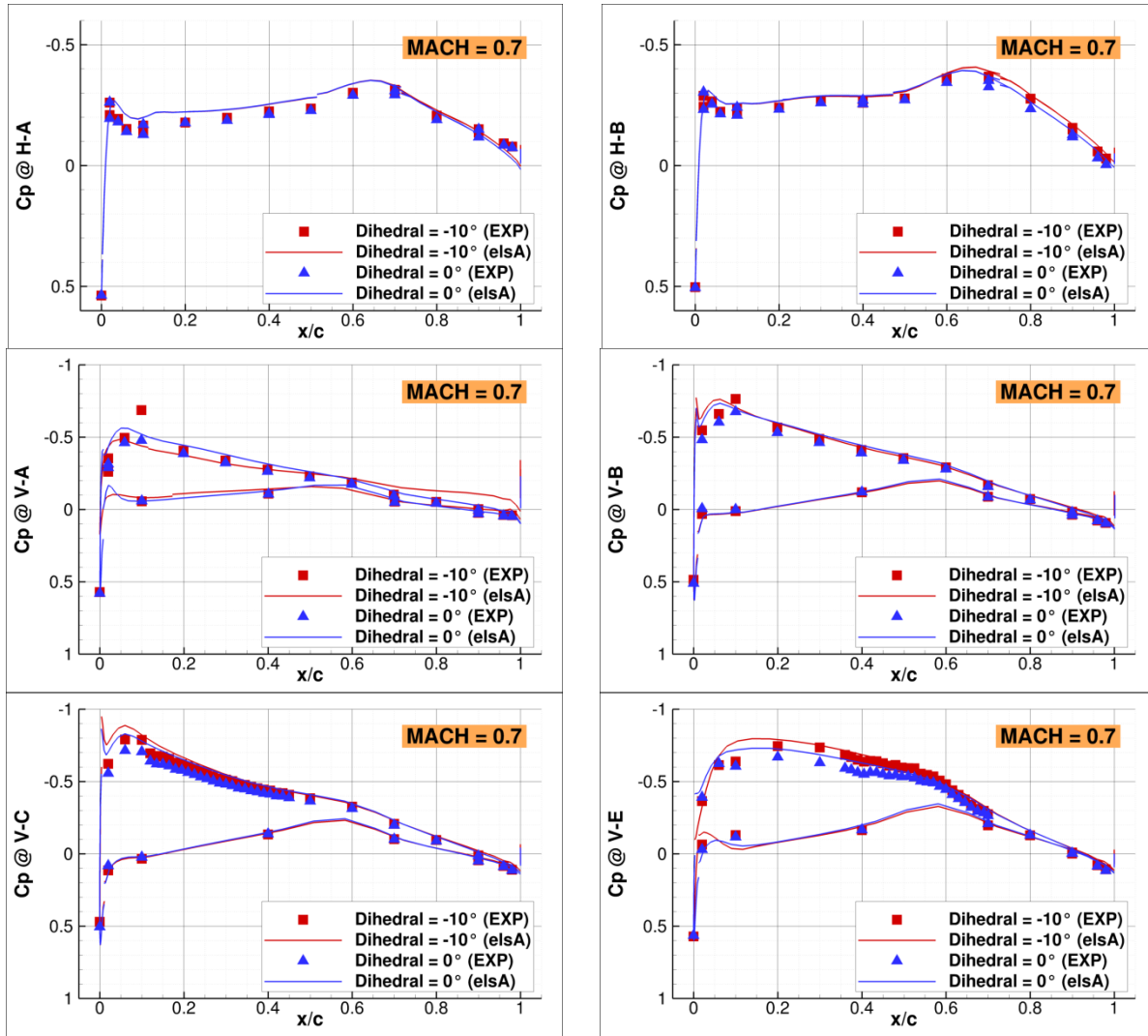


Figure 14: Dihedral effect on experimental and numerical steady pressure coefficients on different HTP and VTP slices at Mach=0.7 and  $P_i = 1.0$  bar with a fixed yaw angle of  $+2^\circ$ .

#### 4.1.2 Unsteady pressure coefficients

The unsteady pressure coefficients have been measured by exciting the flutter model with a time-harmonic pitching motion. Different experimental pressure tests were made at frequencies ranging from 5Hz to 60 Hz, and amplitudes  $0.1^\circ$  and  $0.2^\circ$ , but only the 5Hz /  $0.2^\circ$  pitch motion is considered in the following results.

Dynamic fluid-structure coupling simulations and particularly, harmonic forced motion simulations, have been performed by imposing a pitching movement to the HTP part. The Frequency Response Functions are computed relatively to the excitation signal and the real and imaginary parts of the pressure can be compared to the experimental data. The unsteady pressure coefficients obtained at different HTP and VTP slices are presented in Figure 15, for a Mach number of 0.7. A rather good correlation is obtained for the real part of the pressure coefficients. However, some discrepancies occur for the imaginary part of the pressure which is not well predicted around the HTP / VTP junction (V-E section).

These discrepancies are even more important when increasing the Mach number, as shown in Figure 16, for a Mach of 0.8. The real part of the pressure coefficients is well predicted, except again near the HTP and VTP junction (V-E slice). An attempt of improving the results by adding an injection boundary condition (to take into account the leakages appeared during the wind tunnel tests), is not efficient.

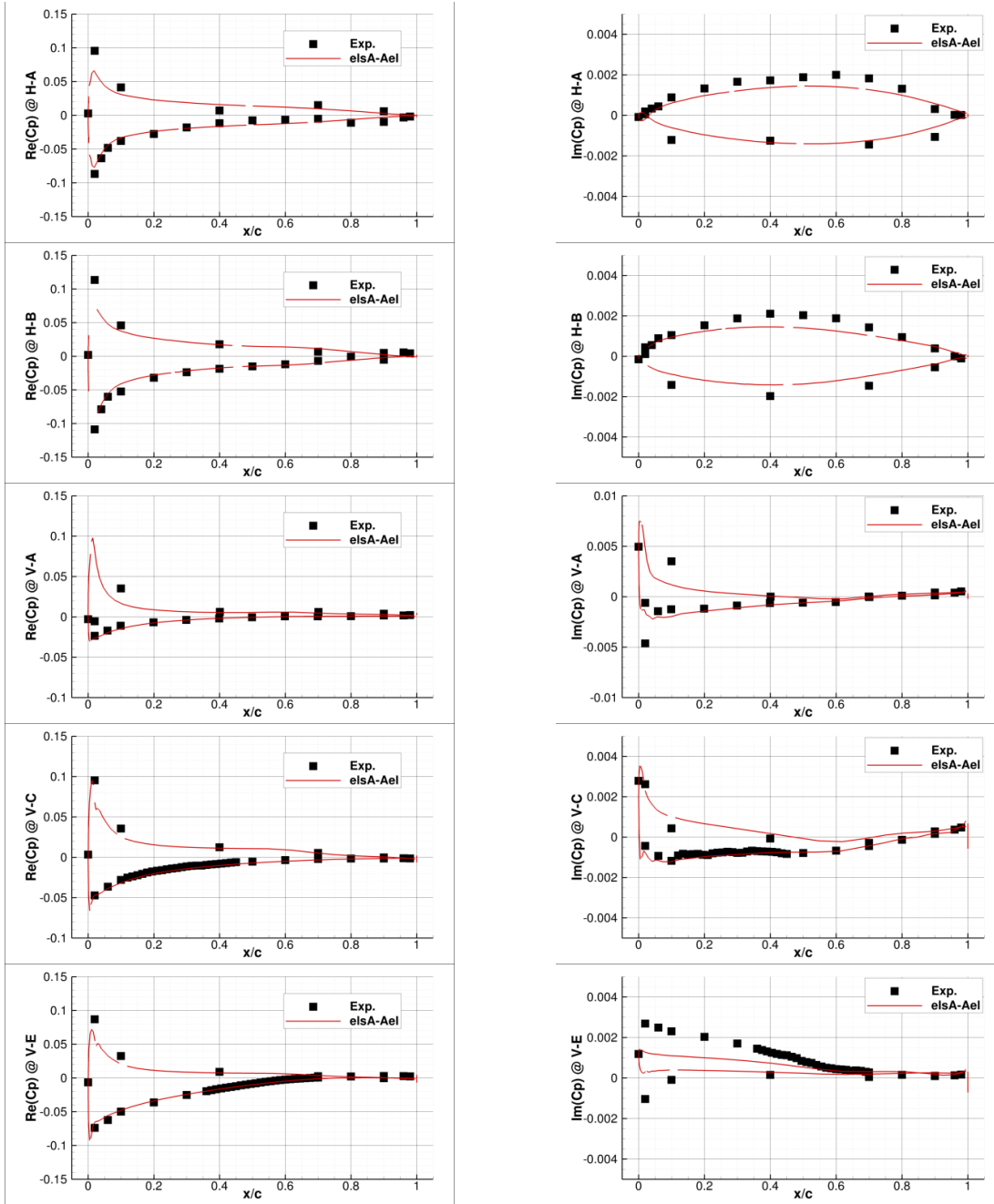


Figure 15: MACH = 0.7 - Experimental and numerical unsteady pressure coefficients on different HTP and VTP slices obtained with a harmonic excitation signal of 5Hz and  $0.2^\circ$  (Yaw angle =  $-2^\circ / 0^\circ$  dihedral).

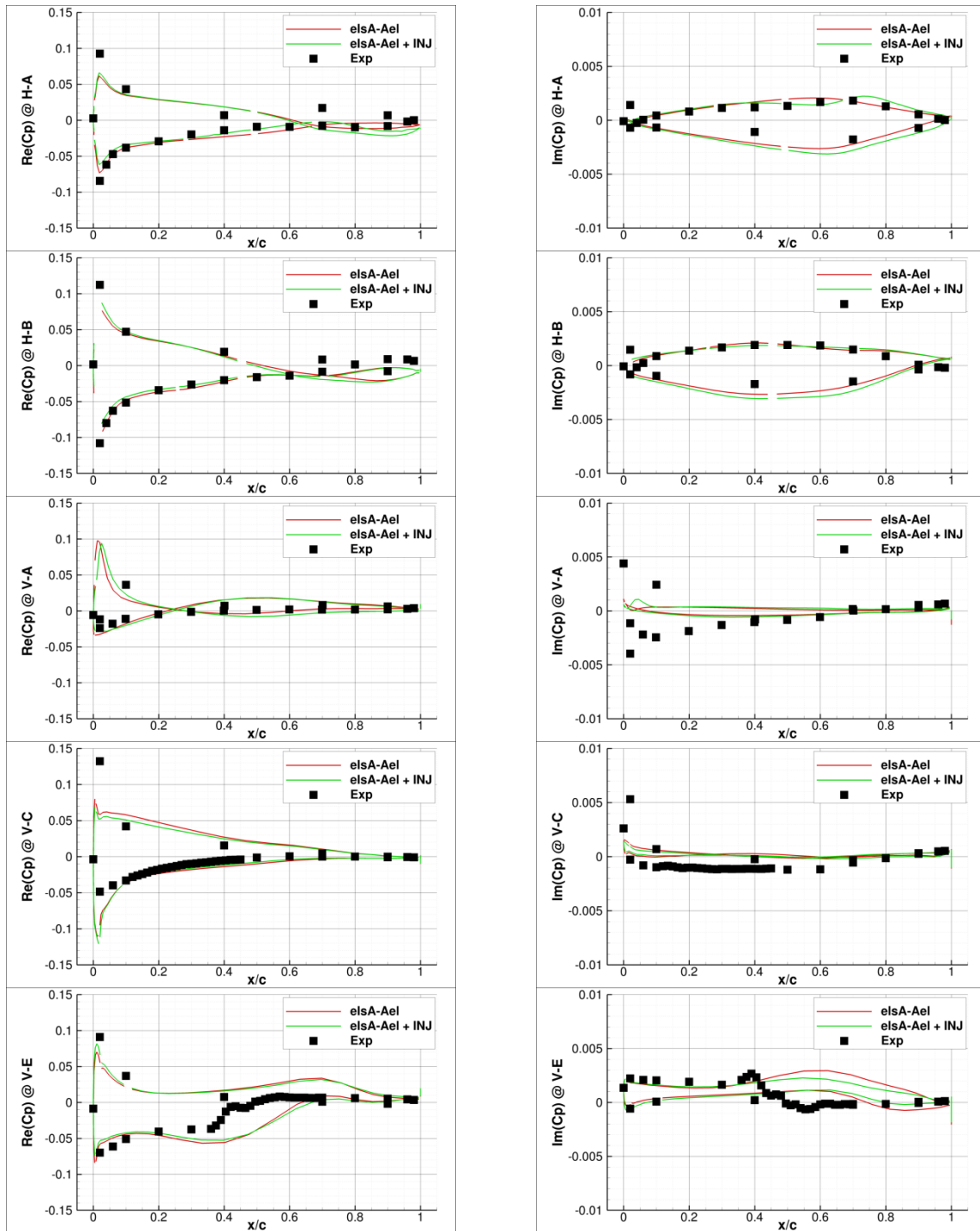


Figure 16: MACH = 0.8 - Experimental and numerical unsteady pressure coefficients on different HTP and VTP slices obtained with a harmonic excitation signal of 5Hz and  $0.2^\circ$ . With and without the injection correction (Yaw angle =  $-2^\circ / 0^\circ$  dihedral)

## 4.2 Flutter diagrams

The different numerical methods previously presented are used to plot the evolution of the modal frequencies and damping ratios with the stagnation pressure. The resulting flutter diagrams are presented in Figure 17 and Figure 18 for the first two structural modes (first bending and first torsion modes of the HTP) for Mach numbers of 0.7 and 0.8. The results obtained correspond to the flutter model with a yaw angle of  $-2^\circ$  and a dihedral of  $0^\circ$ , and the numerical results are compared to the corresponding experimental data.

In Figure 17, the DLM (blue lines) gives a very good correlation with the experimental data and predicts the flutter pressure with only an error of 4%. The Pulse method and the FHEM (green and pink curves) give very similar results with a flutter pressure underestimated by 9%, and show both a very good prediction of the modal frequencies. Then, even if the Direct Coupling method (DCM) (red lines) gives a very good prediction of the flutter pressure (with only an error of 2%), the behavior of the modal frequencies and the damping is not correlated with the other numerical methods and with the experimental data.

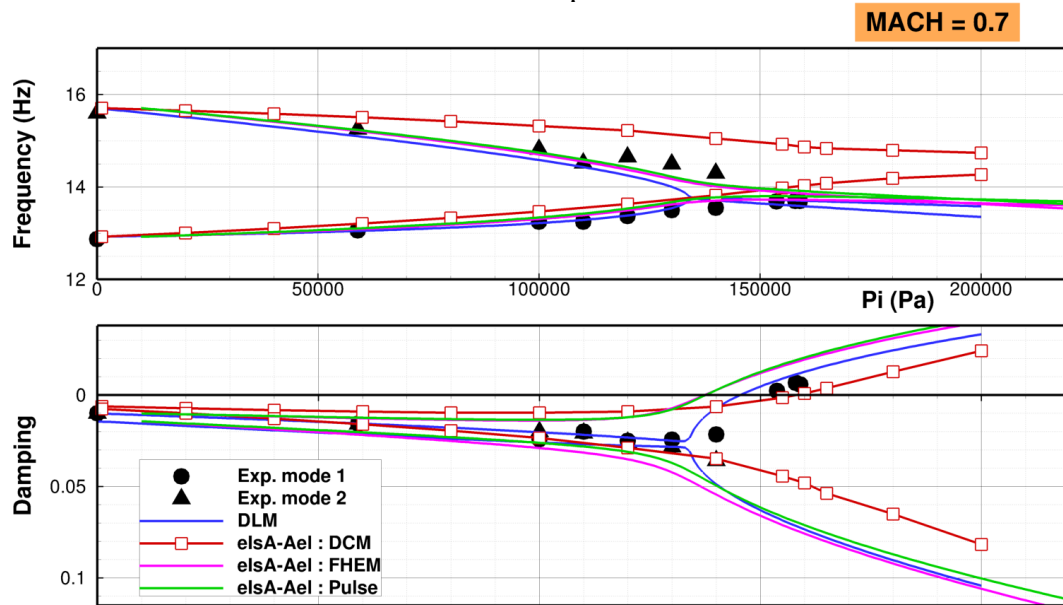


Figure 17: MACH = 0.7 – Flutter diagram: Comparison of the experimental and DLM data with different high-fidelity numerical methods (Direct Coupling, Forced Harmonic Excitation, Pulse methods) (Yaw angle =  $-2^\circ / 0^\circ$  dihedral).

In Figure 18, the increase in Mach number yields to a drop in the flutter dynamic pressure. For this Mach number of 0.8, all the numerical methods predict approximately the same value of the flutter pressure with an underestimation of about 15%. Once again, the Pulse method is able to predict very accurately the evolution of the modal frequencies, contrarily to the DCM. When taking into account a correction for the leakages appeared during the WTT measurements (with an injection boundary condition), the prediction of the flutter pressure can be improved only by 3%.

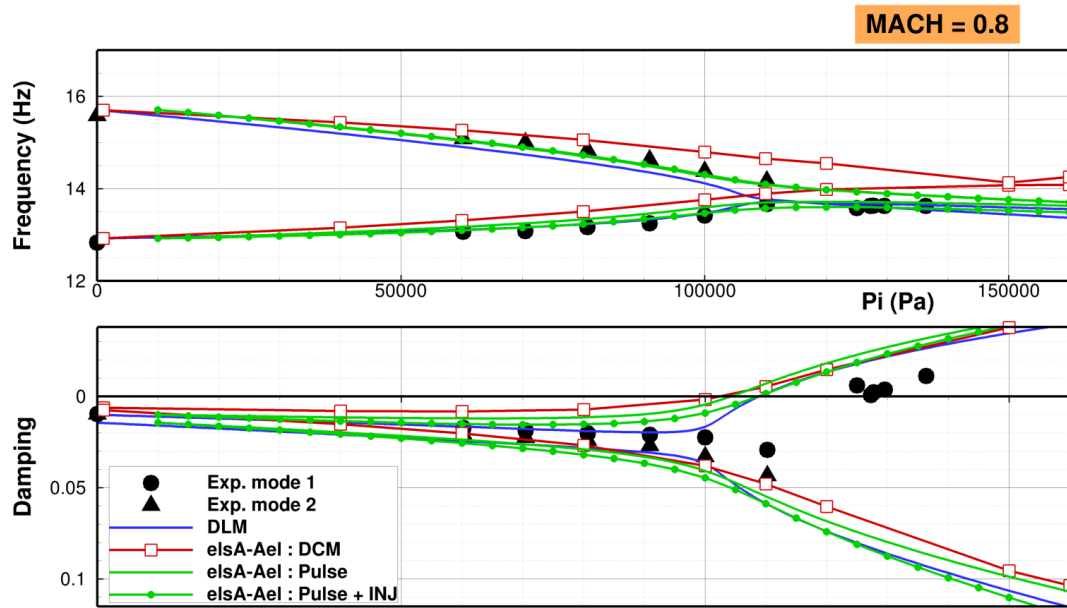


Figure 18: MACH = 0.8 – Flutter diagram: Comparison of the experimental and DLM data with different high-fidelity numerical methods (Direct Coupling, Forced Harmonic Excitation, Pulse methods). With and without injection correction. (Yaw angle =  $-2^\circ / 0^\circ$  dihedral).

#### 4.2.1 Mach effect

Figure 19 shows the evolution of the flutter pressure with the Mach number for the flutter model with a yaw angle of  $-2^\circ$  and a dihedral of  $0^\circ$ . Once again, the DLM gives relatively good correlations with experimental data with an underestimated flutter pressure of from 5 to 15 %, even for high Mach numbers. The high-fidelity numerical tools (DCM and Pulse method) are not able to improve the DLM predictions.

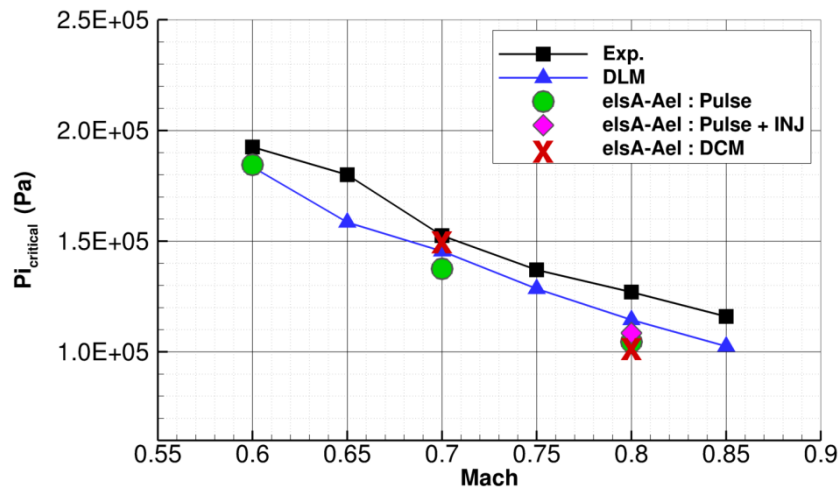


Figure 19: Evolution of the critical pressure with the Mach number. Comparison of the available numerical methods with experimental data. (Yaw angle =  $-2^\circ / 0^\circ$  dihedral).

#### 4.2.2 Yaw angle effect

When the yaw angle is set to  $+2^\circ$ , i.e. when the VTP leading edge is directed towards the fuselage, the flutter pressure is increased up to 2.0 bars. For this configuration, the comparison of our numerical data to the experimental data shows again some important discrepancies. The flutter diagrams in Figure 20 show that the DLM and the Pulse method are not able anymore to predict the good evolution of the modal frequencies and damping ratios

(with an error of prediction higher than 30%). The DCM gives relatively better results (flutter pressure underestimated with an error of 15%) but still does not predict the good flutter behavior.

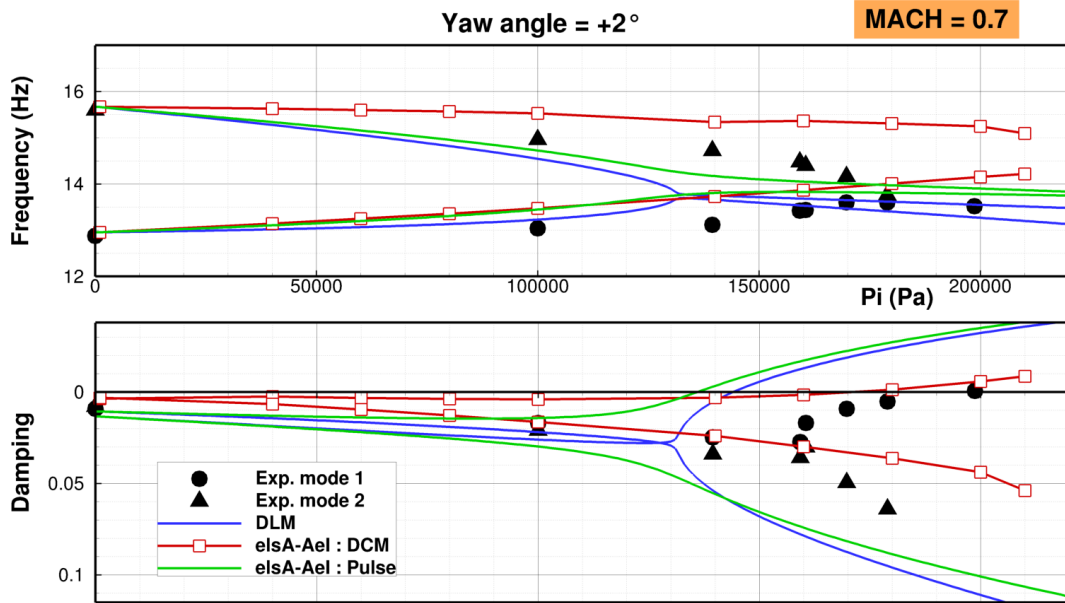


Figure 20: MACH = 0.7 – Flutter diagram : Comparison of the experimental and DLM data with different high-fidelity numerical methods (Direct Coupling, Pulse methods). Without injection correction. (Yaw angle =  $+2^\circ$  /  $0^\circ$  dihedral).

#### 4.2.3 Dihedral effect

As for the positive yaw angle, a negative dihedral increases the flutter pressure because it produces an antisymmetric incidence on the VTP and then yields to a stabilizing moment. For this configuration with a dihedral of  $-10^\circ$ , the flutter diagrams in Figure 21 show that the DLM and the Pulse method have some difficulties to predict the good flutter behavior, in particular they predict both a bad evolution of the modal frequencies. The damping ratios, and then the critical flutter pressure, seem however to be relatively well predicted.

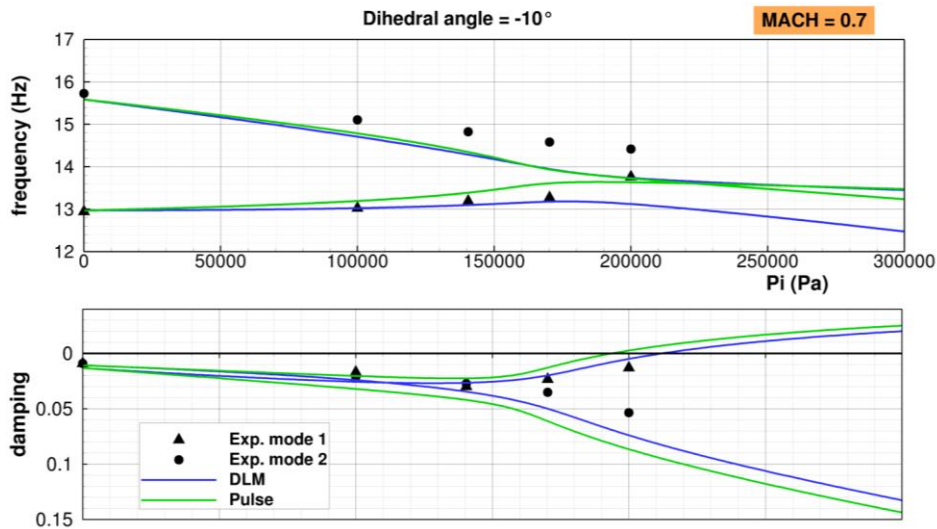


Figure 21: MACH = 0.7 – Flutter diagram : Comparison of the experimental and DLM data with the Pulse method). Without injection correction (Yaw angle =  $+2^\circ$  /  $-10^\circ$  dihedral).

## 5 CONCLUSIONS

The aim of this study was to compare and assess different numerical methods for the flutter analysis of tail configurations, in subsonic and transonic domains. Numerical results obtained with high-fidelity fluid-structure coupling methods such as the Forced Harmonic Excitation, the Pulse and the Direct Coupling methods are compared to Wind Tunnel Test data and to results obtained with the low-fidelity DLM method. Steady and unsteady pressure coefficients are first analyzed and enable to optionally correct our numerical data by adding an injection condition at the junction between the fuselage and the HTP, where some leakages had occurred during the WTT. This correction is particularly applied at a Mach number of 0.8 and slightly improves the prediction of the flutter pressure.

Aerodynamic and flutter correlations between experimental and numerical results are quite good for a tail flutter model involving intersecting surfaces, with a yaw angle of  $-2^\circ$  and a dihedral of  $0^\circ$ . However, for a positive yaw angle of  $+2^\circ$ , the numerical methods are not able to correctly predict the flutter speed. In the same way, for a negative dihedral, the flutter behavior and particularly the evolution of the modal frequencies is not well predicted.

The comparison between the different numerical methods yields to mixed results:

- the results obtained with the DCM are very disappointing for the flutter behavior prediction, whatever the aerodynamic conditions or the flutter model geometry.
- the results obtained with the Pulse method are very promising and show that this method can efficiently replace the more classical, but very time consuming, FHEM.
- the results obtained with the DLM are relatively very good even at high Mach numbers (Mach = 0.8), except for geometries with more complex flow behavior (positive yaw angle, negative dihedral), and show the robustness of this method.

Further work is still required to complete the analysis of the WTT database, and in particular to investigate other flutter model geometries. This could help to better analyze and understand the reasons for the poor results provided by DCM. It would be further interesting to investigate the use of the Quadratic Constitutive Relation (QCR) instead of the Boussinesq relation in the Spalart-Almaras turbulence model in order to better predict the corner flow behavior near the intersecting surfaces.

## 6 REFERENCES

- [1] Flax A., Lawrence H. (1951). The aerodynamics of low-aspect-ratio wings and wing-body combinations, *3<sup>rd</sup> Anglo-American Aeronautics conference*, Brighton, UK.
- [2] Davies D. (1966). Generalized aerodynamic forces on a T-tail oscillating in subsonic flow, *Aeronautical Research Council Reports and Memoranda*, 3422.
- [3] Stark V. (1964). Aerodynamic forces on a combination of a wing and a fin oscillating in subsonic flow, *SAAB TN 54*.
- [4] Albano E., Rodden W.P. (1969). A Doublet Lattice Method for Calculating Lift Distributions on Oscillating Surfaces in Subsonic Flows, *AIAA Journal*, 7(2), 279-285.
- [5] Murua J., Martínez P., Climent H., van Zyl L., Palacios R. (2014). T-tail flutter: Potential-flow modelling, experimental validation and flight tests, *Progress in Aerospace Sciences*, 71, 54-84.
- [6] Geuzaine P., Brown G., Harris C., Farhat C. (2003). Aeroelastic dynamic analysis of a full F-16 configuration for various flight conditions, *AIAA Journal*, 41(3), 363-371.
- [7] Nikbay K., Farhat C. (2001). Coupled analytical sensitivity analysis and optimization of three-dimensional nonlinear aeroelastic systems, *AIAA Journal*, 39(11), 2051-2061.

- [8] Geeraert A., Lepage A., Stephani P., Feldmann D., Häberli W. (2017). Wind tunnel flutter tests of a U-tail configuration. Part 1: Model design and testing. *International Forum on Aeroelasticity and Structural Dynamics*, Como, Italy.
- [9] Mamelle H., Broux G., Garrigues E. (2017). Wind tunnel flutter tests of a U-tail configuration. Part 2: Experimental and numerical results. *International Forum on Aeroelasticity and Structural Dynamics*, Como, Italy.
- [10] Dat, R. and Meurzec, J-L. (1969). On the Flutter Calculations by the so-called “Reduced Frequency Scanning” Method, *La Recherche Aéronautique*, 133, 41-44.
- [11] Tran D.-M., Liauzun C., Labaste C. (2003). Method of Fluid-Structure Coupling in Frequency and Time Domains using Linearized Aerodynamics for Turbomachinery, *Journal of Fluids and Structures*, 17, 1161-1180.
- [12] Cambier L., Heib S., Plot S. (2013). The Onera elsA CFD software: input from research and feedback from industry, *Mechanics & Industry*, 14, 159-174.
- [13] Mortchelewiz G-D, Le Bihan D. (2018). Pulse method for flutter prediction, *58<sup>th</sup> IACAS*, Tel-Aviv, Israël.
- [14] Silva W.A. (1997). Identification of linear and nonlinear aerodynamic impulse responses using digital filter techniques, *NASA Technical Memorandum*, 112872.
- [15] Silva W.A., Raveh D. (2001). Development of unsteady aerodynamic state space models from CFD-based pulse responses, *AIAA Journal*, 1213.
- [16] Fletcher, R. (2003). *Practical Methods of Optimization*, Wiley.

## ACKNOWLEDGMENTS

This project has received funding from Cleansky-2 Joint Undertaking under the European Union's Horizon 2020 research and innovation programme under grant agreement N° CS2-AIR-GAM-2014-2015-01". This paper only reflects the author's view and the CS2 JU is not responsible for any use that may be made of the information it contains.

More specifically, the authors would like to thank Gabriel Broux, Elsa Breus and Nicolas Forestier from Dassault Aviation for their help and fruitful discussions.